FY 2016 FES Theory & Simulation Performance Target

Theory-Simulation members
C. S. Chang (coordinator), R. M. Churchill, R. Hager, S. Ku, and D. Stotler (PPPL);
X. Q. Xu, Bin Chen, B. Cohen, I. Joseph, T. Rognlien, T.F. Tand, and Maxim Umansky (LLNL);
and J. Myra (Lodestar)

Experimental collaborators
R. Maingi (experimental coordinator), J.-W. Ahn and T. Gray (NSTX-U); J. Hughes, B. LaBombard and Jim Terry (C-Mod); T. Leonard and M. Makowski (DIII-D)

Annual target: Predicting the magnitude and scaling of the divertor heat load width in magnetically confined burning plasmas is a high priority for the fusion program and ITER. One of the key unresolved physics issues is what sets the heat flux width at the entrance to the divertor region. Perform massively parallel simulations using 3D edge kinetic and fluid codes to determine the parameter dependence of the heat load width at the divertor entrance and compute the divertor plate heat flux applicable to moderate particle recycling conditions. Comparisons will be made with data from DIII-D, NSTX-U, and C-Mod.

1st Quarter Milestone: Incorporate experimental plasma profiles relevant to the B_{POL} scan

Parameterize time-averaged midplane plasma profiles from available experimental data under attached plasma operation according to the magnitude of the poloidal magnetic field at the outboard midplane; prepare a set of kinetic EFIT output files as needed; and import equilibria into the gyro-Landau fluid BOUT++ and gyrokinetic XGC1 codes. Perform initial 3D electrostatic fluid stability and multiscale gyrokinetic turbulence simulations.

2nd Quarter Milestone: Use XGC1 for the initial turbulence and heat flux width characterization and perform BOUT++ simulations

From massively parallel simulations, characterize underlying blobby electrostatic plasma instabilities predicted by the edge gyrokinetic code XGC1 with respect to the poloidal magnetic field, and determine appropriate models available in BOUT++ based on analysis of relevant underlying plasma instabilities. Perform initial computations of the heat flux width at the divertor entrance using XGC1 and BOUT++ and compare with experimental data.

3rd Quarter: Investigate the role of edge plasma turbulence in divertor heat flux width

Perform more BOUT++ and XGC1 edge turbulence simulations in realistic divertor geometry. Analyze simulation results to obtain basic physics understanding of the role of the electrostatic and electromagnetic turbulence on the divertor heat flux width relative to parallel, neoclassical, radiation and neutral particle physics. Investigate the correlation between the computed midplane plasma profiles and the divertor heat flux width.

4th Quarter: Quantify prediction for the divertor heat flux width scaling under moderate particle recycling conditions

Using the 3rd Quarter results, quantify and predict the divertor heat flux width scaling at the divertor entrance with respect to the poloidal magnetic field and other significant parameters. Investigate the sensitivity of the results to computational resolution and model parameters. Document the simulations and prepare final report.

Completion of the 1st Quarter Milestone

Milestone: Incorporate experimental plasma profiles relevant to the B_{POL} scan

A theory-experiment team has been formed to carry out the performance target milestones. A set of experimental plasma profiles relevant to the B_{POL} scan (equivalently, to the I_P scan) at a fixed toroidal magnetic field B_T for each machine have been provided by all three US major tokamaks: DIII-D for conventional aspect ratio, NSTX for tight aspect ratio, and C-Mod for high magnetic field at conventional aspect ratio. Since the relevant NSTX-U data will not be available in time due to an unexpected delay in the operation schedule, the NSTX data will be used instead. The kinetic EFIT output files containing both the magnetic geometries and the plasma profiles have been provided by the experimental contacts for each device. All cases are for attached divertor operation, pertinent to the present research target. It is not intended that the milestone target research analyzes all of the plasma cases provided the experimentalists, but only those relevant and viable. Some of the cases could have difficult geometries for high fidelity simulation. The experimental conditions considered are:

DIII-D

Shot	Time (ms)	B_T (T)	I_P (MA)
144987	3047	2.1	0.5
144977	3103	2.1	1.0
144981	3175	2.1	1.5

NSTX

Shot	Time (ms)	B_T (T)	I_P (MA)
132368	360	0.4	0.7
127975	410	0.4	1.0
128797	410	0.4	1.2

C-Mod

Shot	Time (ms)	B_T (T)	I_P (MA)
1100303017	1033	5.4	1.0
1100223023	1236	5.4	0.9
1100223012	1149	5.4	0.8
1100223026	1091	5.4	0.5

Table I. Experimental plasma cases provided by experimental partners from three major US tokamak devices.

For the initial study in Q1, which is focused on the rise phase of the edge turbulence and the corresponding divertor heat flux width, we chose the DIII-D shots #144977 and #144981, having medium and high plasma current I_P=1 MA, 1.5 MA, respectively. The linear electromagnetic modes in both discharges have been simulated with the (gyro-Landau) fluid code BOUT++ both with and without the Landau damping and toroidal closures: No significant difference has been found between them. The resulting initial growth stage in the 1.5 MA run is compared with the nonlinear initial growth obtained by the gyrokinetic full-f particle code XGC1 in a nonlinear electrostatic simulation, which naturally includes self-consistent neoclassical physics.

Figure 1 shows the poloidal variation of the pressure perturbation for the linear n=30 mode from the electromagnetic gyro-Landau module in BOUT++. The toroidal mode number dependence of

the linear growth rate is provided in Fig. 2. The 6-field electromagnetic module in BOUT++ yields similar results.
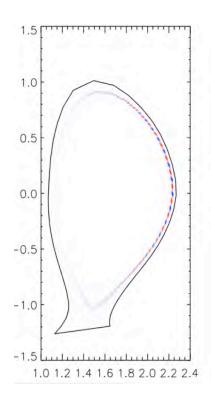

Fig. 1. Poloidal slice through the high current DIII-D H-mode discharge 144981 from BOUT++ in single-null divertor, showing pressure perturbation for dominant toroidal mode number n=30 with the characteristics of the ballooning modes.
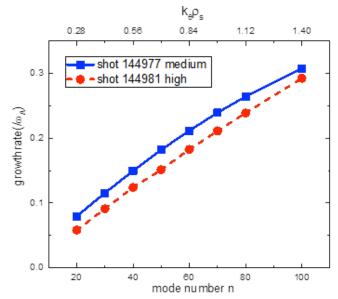

Fig. 2. Toroidal mode spectrum of two DIII-D discharges as calculated by BOUT++ for the following cases: Red for high current and Blue for medium current. The growth rates are normalized to the Alfven frequency $\omega_A=2.3416 \times 10^6/s$

Figure 3 is the toroidal mode spectrum of the high current DIII-D discharge from the hybrid electromagnetic version of XGC1 (called "XGC1-hybrid" in this report). Gyrokinetic ions and fluid electrons are used in XGC1-hybrid. Main difference between this XGC1 simulation and the BOUT++ simulation summarized above is that the ions in XGC1-hybrid are gyrokinetic particles and those in BOUT++ are (gyro)fluid ions. Low to intermediate n-numbers are plotted from XGC1-hybrid in Fig. 3, while intermediate to high n-
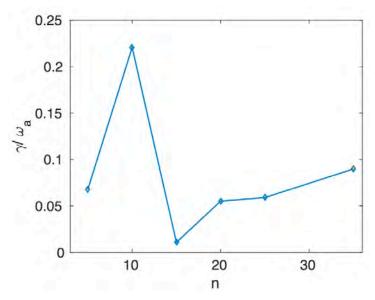

Fig. 3. Toroidal mode number (n) spectrum in the high current DIII-D discharge (144981) from the hybrid electromagnetic calculation in XGC1-particle. Low to intermediate n-numbers are plotted here from XGC1-particle, while intermediate to high n- numbers are plotted in Fig. 2 from BOUT++. In the overlapping intermediate n-numbers (n=20-35), the growth rates from two codes are similar.

numbers are plotted from BOUT++ in Fig. 2. In BOUT++. In the overlapping intermediate n-numbers (n=20-35), the growth rates from two codes are at a similar level. Red data points in Fig. 2 are to be compared with Fig. 3. The lower n-modes with higher growth rate from XGC1-hybrid (Fig. 3) are understood to be kinetic version of the peeling-ballooning like modes. BOUT++ does not see these modes.

Figure 4a depicts the nonlinear density perturbation in the initial growth stage of the nonlinear electrostatic XGC1 particle simulation for the high current case.   In this case, ions are gyrokinetic and the electrons are drift kinetic. In order to distinguish this all-particle simulation from the XGC1-hybrid version, this version of XGC1 is called "XGC1-particle" in this report. Figure 4b contains these same data that are magnified to focus on the outboard midplane area. This XGC1-particle result incorporates the sheared ExB flow, neoclassical particle dynamics, and neutral particle recycling, together with the turbulence, in a self-consistent manner. Enlargement of the region around the outboard midplane in Fig. 4b shows the formation of "blobby" turbulence, showing the source location of the blobs that will eventually occupy the scrape-off region with large electrostatic amplitude.
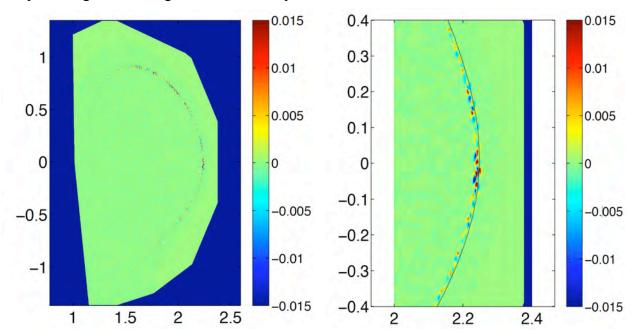

Fig. 4a (left). Initial growth of the normalized density perturbation from a nonlinear simulation in XGC1-particle just inside the magnetic separatrix for the 1.5MA DIII-D case. Fig. 4b (right). Enlargement of the region around the outboard midplane. Penetration of the "blobs" outside of the magnetic separatrix (black curve) is already visual at the outboard midplane.

In the linear BOUT++, the linear XGC1-hybrid, and the nonlinear XGC1-particle simulation results, the n≥20 ballooning mode structures are localized just inside the magnetic separatrix surface, and the growth rates are similar. The low n electromagnetic modes at n≤10 from XGC1-hybrid reside deeper in the pedestal near pedestal top, different from other modes, and will not be discussed further in this Q1 report. There are also differences. The nonlinear XGC1-particle simulation yields modes that are stronger above the midplane, and some of the "blobs" have already traveled outside the separatrix even in the initial growth phase (Fig. 4b, near the outboard

midplane). BOUT++ does see these behaviors. These differences could partially be from the difference in the linear and nonlinear physics. Study of the mode properties will continue. Saturated nonlinear simulations will be performed in Q2-Q4 to obtain the saturated divertor heat-flux width.

Completion of the 2nd Quarter Milestone

Milestone: Use XGC1 for the initial turbulence and heat flux width characterization and perform BOUT++ simulations

The second quarter milestone was met by performing XGC1 and BOUT++ simulations for the initial turbulence and heat flux width characterization. More specifically, the second quarter research activities have been met by performing i) cross-verification of the linear electromagnetic modes between BOUT++ and XGC1, and extension from Q1 of the massively parallel computing study of the nonlinear blobby turbulence and parallel heat flux width in the high current DIII-D case (1.5MA, discharge #144981) using the XGC1 gyrokinetic particle code with drift kinetic electrons, and ii) completion of the DIII-D linear mode studies in the BOUT++ (gyro)fluid code by adding the low current case (0.5MA, discharge 144987) to the medium and high current studies reported in Q1 (see Fig. 2) and by performing a nonlinear examination of the edge modes and divertor heat-flux footprint in the high current C-Mod case (0.9MA, discharge 1100212023).

1) **XGC1 study**:

    1.A) Cross-verification of XGC1's electromagnetic solutions with BOUT++:
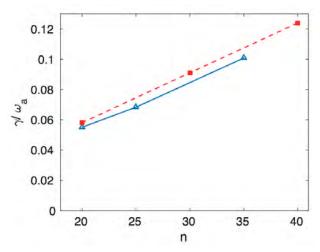

Fig. 5. Cross verification of the electromagnetic modes between XGC1 (blue) and BOUT++ (red) for intermediate to high toroidal mode number n modes. DIII-D discharge at 1.5MA is used.

The electromagnetic XGC1 simulation has been refined to allow cross-verification of the intermediate to high toroidal mode number modes against the BOUT++ results from Q1 (Fig. 2). Figure 5 depicts the excellent agreement between the growth rates obtained by the two codes in the high current (1.5MA) DIII-D discharge for intermediate to high n numbers. As described in the Q1 report, a discrepancy exists, though, at lower n modes, n < 15. XGC1 finds strong growth rates of peeling type, while BOUT++ shows only marginally unstable growth for n<15.

    1.B) Nonlinear simulation of the DIII-D reference cases:

The 27 PF (peak) Titan computer has been used to simulate the DIII-D high current case (1.5MA, discharge #144981), continuing the previously reported linear study into the nonlinear regime. 90% of the maximal Cray-XK7 CPU and GPU have been utilized for a

few days for this simulation. Approximately steady nonlinear blobby turbulence (Fig. 6) and divertor heat-flux footprint have been obtained. Figure 7 shows the smoothed divertor heat-flux footprint measured before entering the Debye sheath at the divertor surface, but after the plasma has fallen through the pre-sheath potential that transfers electron energy to the ions. The power density is per midplane area as is commonly done for experimental data, not per the divertor target area. An application of Eich's fitting technique [Eich13] yields a width of $\lambda_q^{XGC1} \approx 1.8$ mm for this edge plasma. If we evaluate Eich's multi-machine regression formula #14, $\lambda_q^{(14)} \approx 0.63\ B_{pol}^{-1.19}$ mm [Eich13], for the heat-load width, we obtain $\lambda_q^{(14)} \approx 1.77$ mm: an excellent agreement with the XGC1 result.

Fig. 6. Nonliear blobby turbulent δn/n from XGC1, measured at outboard midplane from the DIII-D 144981 simulation.

We can also compare the XGC1 footprint shape against that obtained from IR camera data footprint shape by normalizing the profile peaks to each other by multiplying 1.3 to XGC1 data (Fig. 8). The agreement between experiment (blue) and XGC1 (red) is good, but not perfect at 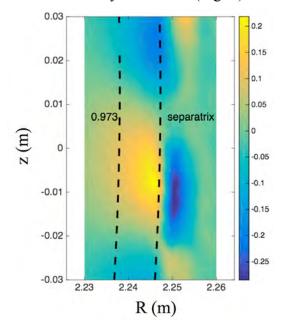the private flux and at far scrape-off regions. The increased experimental heat load (blue) in the private flux region is, however, an artifact of large error in the mapping of the IR data to the outside midplane due to the highly acute incidence angle of the magnetic field lines to the private-flux divertor plates. Lower heat-flux
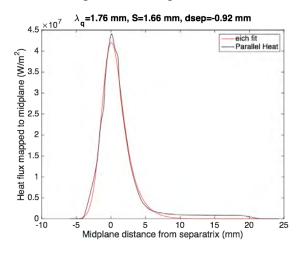

Fig. 7. Heat-flux footprint mapped back to outside midplane on the 1.5MA DIII-D discharge #144981. The Eich formula yields an excellent fit, with $\lambda_q^{XGC1} \approx 1.8$mm.
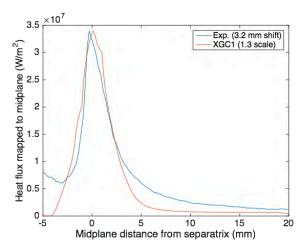

Fig. 8. Heat-flux footprint shape comparison between XGC1 (divided by 1.3) and experiment (moved inward by 3mm) on DIII-D discharge #144981.

at far scrape-off in the XGC1 footprint could be from the grounded potential boundary

condition wherever the magnetic field lines intersect with material wall within distance much shorter than qR. Application of Eich's fitting technique to the experimental IR data (blue) yields λ_q=2.4 mm, which shows a greater deviation from the regression formla that is larger than the XGC1 results ($\lambda_q^{XGC1} \approx 1.8$ mm). The S value from the XGC1 footprint is larger than that obtained from experiment.

The electron and ion contributions to the heat-flux footprint are compared in Fig. 9. Numerical measurement is made at the last grid points in front of the divertor plates, before entering the logical Debye sheath. The footprint is then mapped to the outboard midplane. We caution here that the separation of this footprint into the ion and electron components is for physics understanding purpose only, and not for comparison with actual experimental measurement on divertor plates such as a probe data. In the simplified neutral Monte Carlo routine, we simulate the neutral atoms only without calculating the molecular dissociation into atoms. Thus, it is assumed that the neutral atoms are born at some distance away from the divertor plates, and the atomic interaction of electrons and ions with neutral particles near the divertor plates is missing.
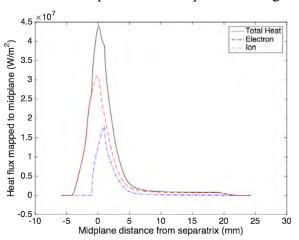

Fig. 9. Comparison of the heat-flux footprint between ions and electrons in the same DIII-D discharge as in Figs. 6-8.

There is a disparity between the ion and electron heat-flux widths even though the particle flux widths are the same to satisfy the gyrokinetic quasi-neutrality and ambipolarity. A detailed examination shows that the wider ion heat profile is due to the larger neoclassical magnetic drift of hot tail ions. Since the neoclassical electron orbit excursion width is negligibly small, the broadening of the electron heat flux footprint in Fig. 9 is the result of blobby turbulence. The dominance of the ion neoclassical orbit width is due partially to higher ion temperature than electron temperature in the edge, the hot non-Maxwellian tail ions from pedestal, the energy transfer from electrons to ions in the pre-sheath, and most importantly, lack of atomic physics interaction with neutral particles near the divertor plates.

2) **BOUT++ study**:

ii.A) BOUT++ Analysis of DIII-D discharges

To complete the linear instability analysis of the three DIII-D discharges begun in Q1 (Fig. 2), the low current, Ip=0.5MA, discharge #144987 has been added to the study. The result is similar to that of the two higher current cases: all three DIII-D edge plasmas are (1) marginally unstable for ideal Peeling-Ballooning modes; (2) stable for electrostatic (GLF) modes using adiabatic electrons, indicating that the DIII-D discharges are stable for electrostatic ITG modes with adiabatic electrons; and (3) have the most unstable mode peaking inside the magnetic separatrix at midplane (driven by the bad curvature) near the

maximum ion temperature gradient. The BOUT++ 6-field electromagnetic module yields similar results. Nonlinear BOUT++ simulations are under way.

ii.B) BOUT++ Analysis of C-Mod discharges

A nonlinear simulation of the high current (Ip=0.9MA, 1100212023) C-Mod discharge has been successfully completed. Since there are no experimental SOL profiles available, we linearly extrapolate the density and temperature profiles into SOL to avoid discontinuity across the separatrix. The profiles for pressure, density and temperature are shown in Figure 10.
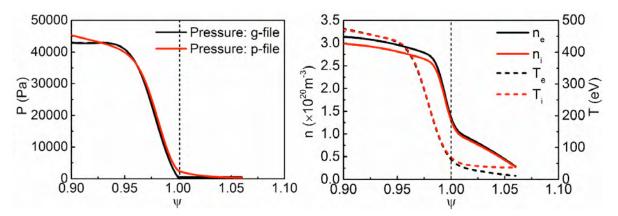

Fig. 10. Profile of (left) total pressure from kinetic EFIT g-file and from measurements in p-file, and (right) electron density and temperatures in pedestal region of C-Mod EDA H-mode #1100212023.

Figure 11 shows the growth rate versus toroidal mode number *n* as calculated by BOUT++ using the electromagnetic GLF module and the 6-field two-fluid models for the C-Mod discharge. Linear simulations show that the EDA H-mode (#1100212023) profiles are dominantly unstable for the resistive ballooning mode (red curve) at the position of peak pressure gradient inside the separatrix, and marginally unstable for the ideal ballooning modes (purple curve). The 3+1 GLF results in the green curve.
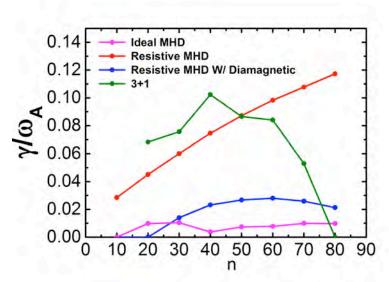

Fig. 11. Toroidal mode spectrum of C-Mod discharge 1100212023 at time 1237ms as calculated by BOUT++. The growth rates are normalized to the Alfven frequency $\omega_A=8.06 \times 10^6/s$.

8

Since this is a typical C-Mod EDA H-mode discharge, the quasi-coherent mode (QCM) is observed in the BOUT++ six-field two-fluid nonlinear simulations with a frequency around 120 kHz, and wavenumber around 1.5 rad/cm as shown in the left panel of Fig. 12, which are consistent with experimental measurements. The right panel of Figure 12 shows the experimental parallel divertor heat flux profile in blue, with the BOUT++ time averaged parallel heat flux profile at the divertor entrance in black and at the divertor target in red.

The BOUT++ simulations suggest that the QCM is localized in the pedestal's peak pressure gradient region just inside the magnetic separatrix. The results also show that the QCMs cause particle and heat to be turbulently transported down their gradients across the separatrix into the SOL, which then flow into the divertor in C-Mod with a rapid relaxation of parallel transport.

In comparison with the experiment, BOUT++ simulations display a qualitatively similar parallel heat flux profile in the near SOL region and a sharp fall-off in the private flux zone. The magnitude of the BOUT++ heat flux is larger, however. The experimental C-Mod heat-flux footprint in Fig. 12 (right) appears closer to a Gaussian shape than those in other machines and those obtained in BOUT++ simulations. But, the spatial resolution of the measurements is limited, while the characteristic length of the fall off of the C-Mod footprint into the private flux region is short. This leads us to infer that the Gaussian-type experimental profile in the private flux region is perhaps broadened by instrumental effects. Moreover, It can also be noticed from Fig. 12 (right) that the heat-flux profile at the divertor entrance (X-point height) is similar to or somewhat broader than that at the divertor target. In addition, there is *a* constant background heat flux in the IR measurement in the far SOL.
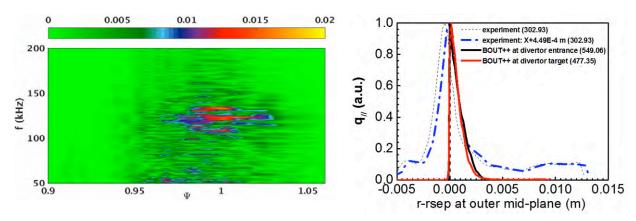

Figure 12. (left) Spectrogram vs radius from BOUT++ simulations for quasi-coherent mode (QCM) of C-Mod EDA H-mode: (right) Radial profile of parallel heat flux mapped to the outer midplane for C-Mod IR-inferred heat flux measurement at outer divertor target (Blue), and from BOUT++ simulations (time averaged) at the outer divertor target (Red) and at the divertor entrance (Black). The experimentally measured parallel heat flux profile (Blue) is shifted outward by ~0.449mm as compared to the simulated particle flux profile. All the parallel heat flux profiles are normalized by the corresponding maximum values. The values in parentheses represent the maximum values in MW/m^2.

Completion of the 3rd Quarter Milestone

Milestone: Investigate the role of edge plasma turbulence in divertor heat flux width

The third quarter milestone was met by performing additional XGC1 and BOUT++ simulations to investigate the role of edge plasma turbulence in setting the divertor heat flux width. In particular, the gyro-kinetic, electrostatic "XGC1-particle" version of XGC1 was used to determine the "blobby", nonlinear, electrostatic turbulent contributions, while the BOUT++ (gyro) fluid code was focused on electromagnetic turbulence. The electromagnetic XGC1-hybrid version was not used in Q3.

XGC1 has been applied to the medium current DIII-D discharge (#144977, 1MA, $B_{pol,mid}$=0.30T) for comparison with the high current DIII-D case (#144981, 1.5MA, $B_{pol,mid}$=0.42T) reported in previous quarters. A high current C-Mod shot (#1100223023, 0.9MA, $B_{pol,mid}$=0.81T) is simulated with XGC1 for comparison with the BOUT++ result from Q2, and an XGC1 run of a high current NSTX discharge (#128797, 1.2MA, $B_{pol,mid}$=0.26T) has been initiated to provide a result at tight aspect ratio. To go with the high and low current BOUT++ runs on DIII-D (#144981, 1.5MA; and #144987, 0.5MA) described in Q1 and Q2, simulations of a medium current DIII-D discharge (#144977, 1MA), and high and medium current C-Mod shots (#1100212023, Ip=0.9MA; and #1100223012, Ip=0.8MA) have been performed in BOUT++.

Combined results from XGC1 and BOUT++ show that the resistive-ballooning modes in the electrostatic branch are important drivers of the edge turbulence. BOUT++ also indicated that the quasi-coherent modes could contribute to the spread of the C-Mod heat-flux footprint.

XGC1 finds that the blobby turbulence does not have a dominant influence over the background neoclassical kinetic orbit drift effect on the divertor heat-flux footprint in the DIII-D and NSTX discharges. On the other hand, interestingly, XGC1 finds that the blobby turbulence has a significant effect over the kinetic neoclassical effect on the heat-flux footprint in the high current C-Mod discharge. This interesting finding on C-Mod could be from two physics effects: the extremely small ion mangetic-drift width compared to the blob size and the formation of a positive potential hill around the magnetic X-point. Both physics effects could have a significant implication in understanding and predicting the divertor heat-flux width for ITER plasmas, and will be investigated further in Q4.
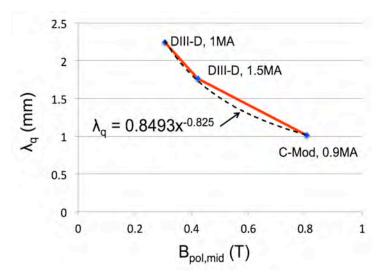
The electromagnetic BOUT++ simulations find that (1) Simulated divertor heat flux widths are in reasonably good agreement with the C-Mod and DIII-D experimental measurements, but the magnitudes of divertor heat fluxes can be different from experimental measurements. Longer simulations in time at least to the order of ion toroidal transit time will be needed to fully resolve the issues; (2) Turbulence dominates over magnetic drifts in radial transport fluxes for both DIII-D and C-Mod discharges; (3) the large SOL turbulence is originated from peak gradients in pedestal, not local instabilities in the SOL; (4) Due to the low toroidal field in NSTX, linear mode growth rates peak at a rather high value of poloidal wavenumber $k_{pol} \rho_i \sim 3$, where $\rho_i = 5$ mm is the value corresponding to experimental measurements in the steep gradient region of the pedestal, which will stress the capabilities of present gyro-Landau fluid theoretical models which begin to lose accuracy when $k_{pol} \rho_i > 1$.

The so-called 2-point model relation of the pressure e-folding length at outboard midplane to Eich's divertor heat-flux width (Eich's λ_q) has not been confirmed by either BOUT++ or XGC1. In some cases, the pressure e-folding length at outboard midplane could be much greater than

Eich's λ_q in BOUT++. Since this is an important topic in validating reduced models, the study will continue to Q4.

1) XGC1 study

Third quarter XGC1 work focused on the contributions of nonlinear blobby turbulence, the predominantly electrostatic fluctuations driving transport in the vicinity of the magnetic separatrix, to the divertor heat load width. The electrostatic XGC1-particle version code was used for this work. Study of the electromagnetic turbulence was left for BOUT++. As reported in the previous quarters, the blobby turbulence in the cold edge plasma is largely associated with the resistive ballooning mode in the electrostatic branch.

Fig. 13. XGC1 simulation results of the Eich heat-flux width λ_q from three different data points over two different tokamaks. Both the magnitude and the $B_{pol}^{-\gamma}$ trend of λ_q agree qualitatively well with the experimental database shown in Fig. 14.

Fig. 14. The trend $\lambda_q \propto B_{pol}^{-\gamma}$ seen from experimental data on existing tokamaks. γ is on the order unity. [T. Eich, Nucl. Fusion, 2013]

The three extreme scale XGC1 simulations of C-Mod, DIII-D and NSTX shots, using 90% of the maximal 27PF Titan CPUs and GPUs at OLCF, consumed more than 150M CPU hours which was much above the allocated ALCC time on Titan. The resulting scaling of the divertor heat flux width with the poloidal magnetic field is depicted in Fig. 13; the corresponding trend from experimental data is shown in Fig. 14. Both the magnitude and the $B_{pol}^{-\gamma}$ trend, with $\gamma \sim 1$ ($\gamma=1.19$ in Eich's regression #14 shown as solid line in Fig. 14), of the Eich width λ_q from limited number of Q3 XGC1 results agree qualitatively with those in the experimental data. A more complete and quantitative scaling study will be performed in Q4. A key new result from these Q3 XGC1 simulations, examined in more detail below, is that blobby turbulence is as significant as neoclassical magnetic drift effect in setting λ_q in the high current C-Mod discharge, while its role is non-dominant in DIII-D (and NSTX), as was reported in previous quarters. The reason why λ_q in C-Mod follows a similar $B_{pol}^{-1.19}$ trend as in the neoclassical physics dominated DIII-D and NSTX systems is an interesting, and potentially critical, question to be investigated in Q4.

11

More detailed Q3 results are summarized as follows:
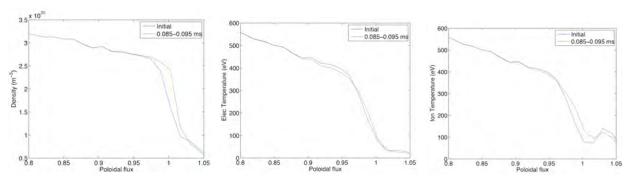
1.A) XGC1 study of a high current C-Mod discharge

Fig. 15. Plasma profiles in the edge region of C-Mod discharge #1100223023 at 0.9MA (n_e, T_e, and T_i from left to right). Blue lines are the inputs to XGC1, which are somewhat arbitrary at $\Psi_N \gtrsim 1$ as explained by BOUT++ section in Q2, and the green lines are the edge profiles found by XGC1.

A higher current C-Mod discharge (#1100223023, Ip=0.9MA) has been examined with XGC1 in Q3 for comparison with the BOUT++ result described above in the Q2 section. The input plasma density, electron temperature, and ion temperature profiles are shown as blue lines in Fig. 15, and are similar to those used by BOUT++ as far as the relevant near SOL is concerned. The bump in the ion temperature profile at far scrape-off layer is a local non-conforming interpolation artifact and do not affect the heat-flux width calculation. While the core plasma profiles are well constrained by experimental measurements, adequate data are not available for $\Psi_N \gtrsim 1$, and the initial input edge plasma profiles are thus somewhat arbitrary. The XGC1-evolved plasma profiles, self-consistently with transport, are shown in green in Fig. 15. The largest difference between the artificial input plasma profiles and the XGC1-found profiles is for the electron density; the XGC1-found density profile has most of the steep gradient region at $\Psi_N \gtrsim 1$ due to the opacity of the edge plasma to neutral particles in this high current C-Mod
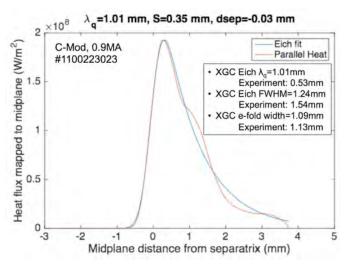

Fig. 16. Divertor heat-flux footprint, mapped back to outboard midplane as calculated by XGC1 for the higher current C-Mod discharge #1100223023.
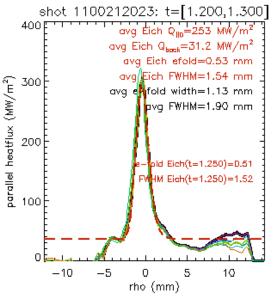

Fig. 17. Experimental heat-flux footprint analysis for C-Mod #1100223023.

discharge.

The parallel heat-flux footprint from the XGC1 simulation, mapped to the outboard midplane, is depicted in Fig. 16. The peak heat flux from XGC1 is about a factor of 1.5 smaller than the experimental value. The Eich formula fits the XGC1 shape well, and the Eich-formula fit λ_q=1.01 mm (Fig. 16) is greater than the experimental result of 0.56mm (Fig. 17). However, the XGC1 simulated λ_q is closer to the Eich's regression-fit value than the experimental value is. This is primarily because XGC1 does not produce the large inward spread of the heat flux into the private flux seen in the experimental data (overlaid in Fig. 18 with the XGC1 heat flux scaled by 1.59). It was told by the C-Mod experimental partner that the experimental
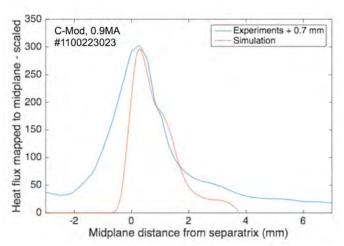

Fig. 18. XGC1 footprint (orange) does not show a large spreading into the private flux region, as seen in the experimental infrared profile (blue), while the outward e-folding length agrees well.

inward spread of the footprint is not to be trusted due the acute angle of the IR cameral to the divertor surface. In Eich's interpretation, such an artificial inward spreading increases the value
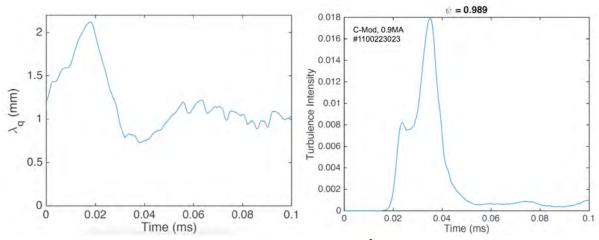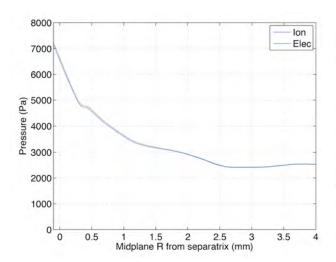

Fig. 19. Saturation of λ_q (left) and turbulence intensity $(\delta n/n)^2$ (right). Turbulence intensity is plotted at $\Psi_N \approx 0.99$ where most of the blobs are born.

of the S parameter in the fit at the expense of λ_q.

The temporal evolution of λ_q and the turbulence intensity near the separatrix are shown in Fig. 19. The kinetic λ_q saturates quickly due to the presence of large sources, sinks and collisions on the ion transit time scale in a non-thermal edge plasma, a feature that is difficult to reproduce in a fluid model with diffusive closures. In comparison, the core plasma's nonlinear turbulence saturation time is about 10 times longer (10^0ms instead of 10^{-1}ms).
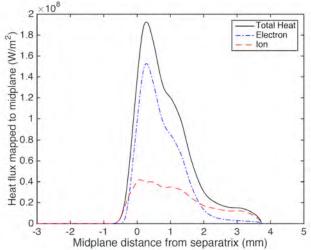
Fig. 20. Upstream electron and ion pressure profile at outboard midplane in the 0.9MA C-Mode simulation, as observed in XGC1.

Fig. 21. Electron contribution from turbulence effect is dominant over ions contribution in the 0.9MA C-Mod simulation.

Figure 20 depicts the ion and electron pressure profiles at outboard midplane for $\Psi_N \geq 1$ found from XGC1; the ion and electron pressure profiles are virtually identical due to the strong collisional coupling. The pressure profile at outboard midplane is so broad that an e-folding length cannot be defined, while the divertor heat-flux footprint falls off nicely and yield a good e-folding length. It appears that the blobby turbulence remove the broad tail pressure part before plasma reaches the divertor plates. Thus, a two-point model relation between the upstream and downstream plasma could not be established is this case where the neutral penetration is shallow and blobby spread is important. This observation is, however, not universal. As can be seen in the next subsection, there is a reasonable relation in the 1MA DIII-D discharge where neutral penetration is deeper and blobs are not the dominant mechanism for the heat-flux broadening.

A peculiar feature in this 0.9MA C-Mod simulation is that the divertor heat-flux width is significantly affected by blobby turbulence, as evidenced by the large contribution of the electron heat flux to the footprint shown in Fig. 21. This was not the case in the DIII-D and NSTX plasmas that have been studied so far. Determining why λ_q on C-Mod follows a $B_{pol}^{-\gamma}$ trend similar that exhibited by the neoclassical physics dominated DIII-D will be interesting and important for ITER. We emphasize here again that the separation of the heat-flux width to electron and ion component is not to be compared with experiment in front of divertor plates due to lack of neutral atomic physics in the simulation near the divertor plates.

Another interesting characteristic of this XGC1 simulation of 0.9MA C-Mod discharge is a positive potential hill around the X-point relative to the flux-surface average potential. Figure 22 shows the mean electrostatic potential variation in
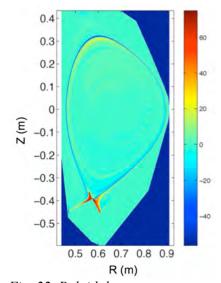

Fig. 22. Poloidal mean electrostatic potential variation in the edge of the 0.9MA C-Mod discharge, after the flux-surface-averaged potential is removed.

14

the edge plasma after subtracting the flux-surface averaged value. The positive potential on the order 50eV around the X-point will give a density hill and, also, may act as a "bumper" to the ion parallel flow from upstream to down stream. Experimental validation of this positive potential hill around the X-point could have significant implications for divertor heat-flux footprint physics.

1.B) XGC1 study of the medium current DIII-D discharge

The medium current DIII-D shot #144977 (1MA, $B_{pol,mid}$=0.30T) was added for comparison with the 1.5MA DIII-D shot. Figure 23 depicts the Eich formula fit, yielding λ_q=2.24mm and S=2.11. The XGC1 and experimental infrared (IR) camera footprints (Fig. 24) yield similar half-widths. However, the larger value of S obtained in the XGC1 Eich fit results in a smaller λ_q than in the fit to the experimental data. In the end, λ_q=2.24mm from XGC1 fits Eich's regression #14 formula, $\lambda_q^{(14)} \approx 0.63\ B_{pol}^{-1.19}$ mm = 1.01 mm, better than the experimental data point does. A factor of 1.14 has been applied to the XGC1 profile height in Fig. 24 to facilitate the width comparison. The unusually high IR camera data in the private flux region is known to be the result of an error
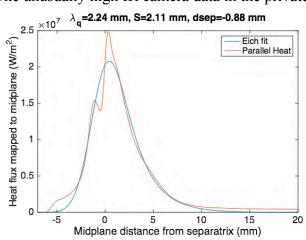

Fig. 23. Eich formula fitting of the divertor heat-flux width for the DIII-D 1MA discharge #14497.
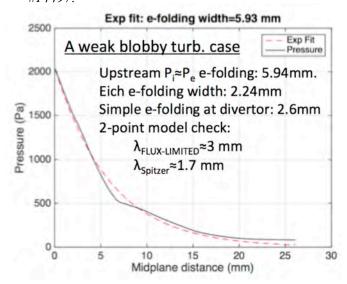

Fig. 24. Comparison of the divertor heat-flux footprint between experiment and XGC1 for the DIII-D 1MA discharge

Fig. 25. Test of the two different popular 2-point models using the XGC1 data on 1MA DIII-D plasma.

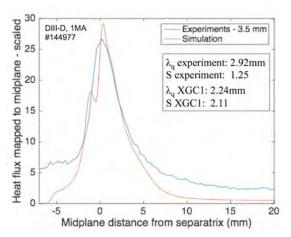in mapping the flux expansion to midplane, as confirmed by the DIII-D experimental partners: The B-field incidence angle to the private-flux divertor plantes is too acute and $d\Psi_N/dR$ in the private flux region along the divertor plate can be too small to produce a reliable mapping to midplane. As in the high current case reported in Q2, the ion neoclassical physics dominates over blobby turbulence in producing the divertor heat flux profile.

In the quest for the relation between the upstream and downstream pressure e-folding length, we plot the outboard midplane pressure profile and compare the e-folding length with the divertor heat-flux

width in Fig. 25. Two popular models (flux-limited and Spitzer) have been used to relate the upstream e-folding length to the divertor footprint width mapped to outbard midplane, as shown in Fig. 25. It is found that the both models give sensible ballpark numbers in the 1MA DIII-D discharge case where the blobby turbulence mechanism is non-dominant in setting the divertor heat-flux width.

1.C) XGC1 study of the high current NSTX discharge

An XGC1 simulation of an NSTX shot (#128797, high current, 1.2MA, $B_{pol,MP}$=0.26T) has begun in Q3. Figures 26a and 26b show the Eich fit to the XGC data and comparison with the experimental IR data. Simulation of NSTX discharges in XGC1 has been difficult due to the large flux expansion, requiring trial and error approach to determine the number of particles needed for stable and reliable solution. A significant of amount of Titan computing time has been spent. Unfortunately, the magnetic field geometry for this NSTX discharge #128797 that was provided to the simulation team was erratic, and the result could not be used in the scaling study. A corrected magnetic geometry has been provided by the NSTX experimental partners. However, this study will not be repeated in Q4 due to lack of computing resources, unless this becomes an essential study-case in quantifying the scaling behavior.
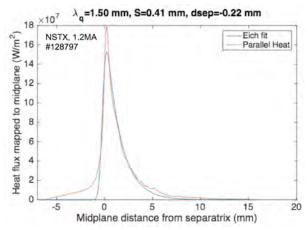

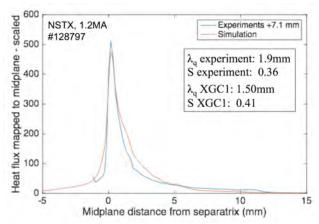*Fig. 26a. Fitting of the XGC1 data from the NSTX 1.2MA discharge simulation to the Eich formula.*

Fig. 26b. Comparison between the XGC1 footprint and the IR camera footprint for the NSTX 1.2MA discharge. The agreement is quite

2a) BOUT++ Analysis of DIII-D discharges

As reported in the last quarter, three DIII-D discharges have been studied. They are shot numbers 144987 for low current Ip=0.5MA, 144977 for intermediate current Ip=1 MA and 144981 for high current Ip=1.5 MA. The BOUT++ simulations show the following characteristics.   The DIII-D magnetic and plasma profiles are (1) marginally unstable for ideal Peeling-Ballooning (P-B) modes; (2) stable for electrostatic GLF simulations with adiabatic electrons, indicating that the DIII-D discharges are stable for electrostatic ITG modes with adiabatic electrons. (3) The most unstable P-B mode peaks inside the magnetic separatrix near the position of peak ion temperature gradient and at the outside midplane, driven by the bad curvature. In addition, the BOUT++ 6-field electromagnetic module is also used for the linear calculations; and the results are similar. The nonlinear BOUT++ simulations are under way. Figure 27 (left) shows the time history of the rms amplitude of electron temperature fluctuation at outside midplane for discharge 144977 with current Ip=1 MA. Figure 1 (right) shows the profile of the electron heat flux at the divertor target. The heat flux width λ_q is almost the same between experimental measurements and BOUT++ simulations, where by λ_q is calculated from the e-folding length of the electron divertor heat flux. $\lambda_q^{BOUT++} = 7$mm, $\lambda_q^{DIII-D} = 7.48$mm. However, the peak divertor heat flux from simulation is 3.6 times larger than experiments. Additional simulations are being performed.
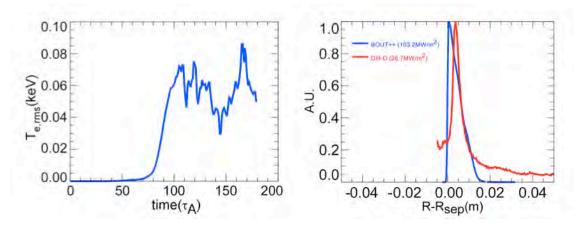

Figure 27. (left) BOUT++ time history of the rms amplitude of electron temperature fluctuation at outside midplane for discharge 144977 with current Ip=1 MA: (right) Radial profile of parallel heat flux mapped to the outer midplane for DIII-D IR-inferred heat flux measurement at outer divertor target (Red), and from BOUT++ simulation (time averaged) at the outer divertor target (Blue). All the parallel heat flux profiles are *normalized by the corresponding maximum values*.

2b) BOUT++ Analysis of C-Mod discharges

In addition to DIII-D, two C-Mod discharges have been successfully simulated. They are shot numbers 1100212023 for high current Ip=0.9MA and 1100223012 for medium current Ip=0.8MA. Since there are no SOL profiles available, we linearly extrapolate the density and temperature profiles into the SOL to avoid a discontinuity across the separatrix. The corresponding profiles of pressure and temperature are shown in Figure 28 for three discharges. Linear simulations show that the EDA H-mode profiles are dominantly unstable for the resistive ballooning mode at the position of peak pressure gradient inside the separatrix and marginally unstable for the ideal ballooning mode. Since this is a typical C-Mod EDA H-mode discharge, the quasi-coherent mode (QCM) is observed in BOUT++ six-field two-fluid nonlinear simulations with frequency around 120 kHz, and k_θ around 1.5 rad/cm, which are consistent with experimental measurements, as reported in the 2nd quarter report. BOUT++ simulations suggest that the QCM is localized in the pedestal
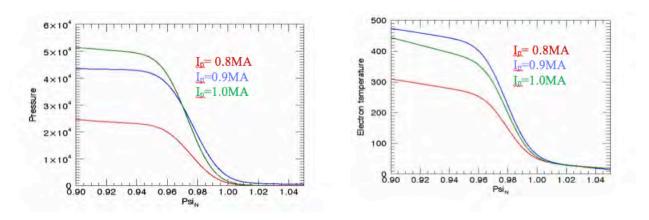

Figure 28. Profiles of total pressure (left) from kinetic EFIT g-file, electron temperature (right) in pedestal region of C-Mod EDA H-mode, linearly extrapolated into the SOL.

peak pressure gradient region inside the magnetic separatrix. BOUT++ nonlinear simulations show that the resulting QCM's cause turbulent particle and heat transport down the gradients across the separatrix into the SOL, which then flow into the divertor in C-Mod driven by a rapid parallel transport.

In comparison with the experiments, BOUT++ simulations display a shape for the parallel heat flux that is qualitatively similar to that typically observed in many tokamaks with a sharp fall-off in the private flux zone. BOUT++ simulations also yield larger amplitudes and narrower widths than in the C-Mod experimental data. The C-Mod heat-flux footprints look more Gaussian than those in other machines and in BOUT++ simulations, but the measurements have poor spatial resolution; and the characteristic length of the fall off of the C-Mod footprint into the private flux region is short. Thus the experimental profile into the private flux is perhaps broadened by instrumental effects.

In this quarter, we performed the flux driven simulations, where the particle and heat sources are included to keep plasma profiles frozen inside the peak gradient position while allowing the plasma profiles to evolve self-consistently outside, including the SOL profiles. Figure 29 shows the time history of rms amplitude of pressure fluctuation at outside midplane at peak gradient position for discharge 11002120023 with current Ip=0.9MA (left) and for discharge 11002120023 with current Ip=0.8MA. Figure 30 shows the pressure profiles at outside midplane at different times for discharge 11002120023
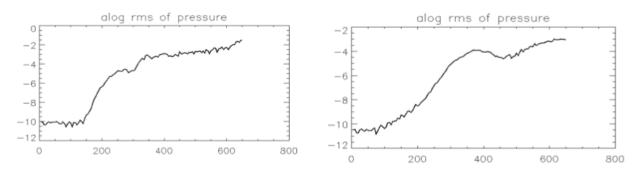

Figure 29. The time history of rms amplitude of pressure fluctuation at outside midplane for discharge 11002120023 (left) with current Ip=0.9 MA and 1100223012 (right) with current Ip=0.8 MA.

(left) with current Ip=0.9 MA and 1100223012 (right) with current Ip=0.8 MA. Due to the radial turbulent transport and magnetic drifts with rapid parallel transport in the SOL, the radial plasma profiles self-consistently evolve in the SOL. BOUT++ simulations display a parallel heat flux that is similar in shape to the Eich fit as shown in Fig. 31, for discharge 11002120023 (left) with current Ip=0.9 MA and 1100223012 (right) with current Ip=0.8 MA. The widths of divertor heat fluxes are consistent with C-Mod experimental data for both cases (not shown). The magnitude of the parallel divertor heat flux is also consistent with C-Mod experimental data for Ip=0.9MA. However, the simulated divertor heat flux is smaller than that in the experiment for Ip=0.8MA: possibly the simulation time is not long enough to conduct all the mid-plane power to the divertor. Both simulations are continuing. The widths of the midplane parallel heat flux, electron density and temperature are shown in Table 1, calculated from the e-folding lengths of the corresponding profiles. For high current Ip=0.9MA, from Eich fit as from Fig.31 (left) we have $\lambda_q^{BOUT++} = 0.81$mm, S=0.13mm, q_0^{BOUT++}=189.9MW, while the C-Mod experiment $\lambda_q^{C-Mod} = 0.53$mm and q_0^{C-Mod}=300MW. For medium current Ip=0.8MA, from Eich fit we have $\lambda_q^{BOUT++} = 0.97$mm, S=0.27mm, q_0^{BOUT++}=0.25MW, the C-Mod experiment $\lambda_{q,}^{C-Mod} = 0.57$mm, q_0^{C-Mod}=200MW. The heat flux amplitude for Ip=0.8MA is much smaller than C-Mod experimental value, possibly due to the fact that the simulation time is not long enough yet.
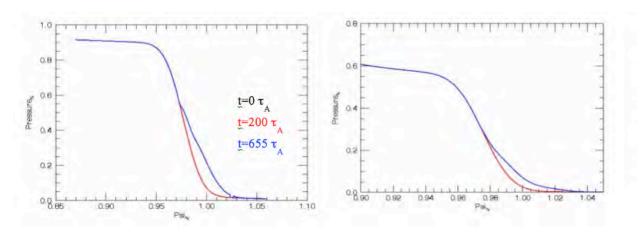
Figure 30. The pressure profiles at outside midplane at different times for discharge 11002120023 (left) with current Ip=0.9 MA and 1100223012 (right) with Ip=0.8 MA.
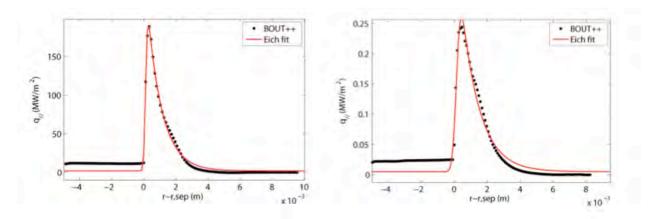

Figure 31. The profiles of parallel divertor heat fluxes for discharge 11002120023 (left) with current Ip=0.9 MA , and 1100223012 (right) with Ip=0.8 MA.

Table 1. C-Mod Bout++ Divertor heat flux widths without sheath boundary condition (preliminary)

	Ip=0.9MA	Ip=0.8MA
λ_{ne}	5.56	8.14
λ_{Te}	4.05	5.37

In conclusion, the two preliminary C-Mod BOUT++ simulations show that the divertor heat flux widths are consistent with 1/Ip scaling.

2c) BOUT++ Analysis of NSTX discharges

Linear BOUT++ simulations of the NSTX discharges have been performed. These plasmas are relatively close to linear marginal stability, which makes the initial-value BOUT++ simulations very challenging and nonlinear simulations even more difficult. Detailed linear stability analysis using the 6-field drift MHD model for the high current I_p = 1 MA discharge #128797 is shown in Fig. 32. The resistive ballooning model with a realistic Spitzer resistivity profile yields the instability shown in Fig. 32(a) with a relatively small growth rate that is maximized as the toroidal mode # n tends toward infinity and tends toward the value ~$0.1/\tau_A$, where the normalization time is τ_A = 2.85×10^{-7} s. After turning on the diamagnetic correction in the vorticity equation, the high n modes shown in Fig. 32 (b) are stabilized, and the maximum growth rate $0.47/\tau_A$ is observed for n = 90. Due to the low toroidal field in NSTX, this corresponds to a rather high value of poloidal wavenumber $k_{pol}\,\rho_i \sim 3$, where ρ_i = 5 mm is the value corresponding to experimental measurements in the steep gradient region of the pedestal. This implies that interactions between electron scale and ion scale physics is likely to be important for these cases. This extremely fine scale structure will stress the capabilities of present gyro-Landau fluid theoretical models which begin to lose accuracy when $k_{pol}\,\rho_i > 1$. For both of these scans, numerical issues are observed to pollute the eigenfunctions at low n < 50 and care must be taken in interpreting the results for low n. Work to eliminate such issues and to continue simulations into the nonlinear regime is ongoing.
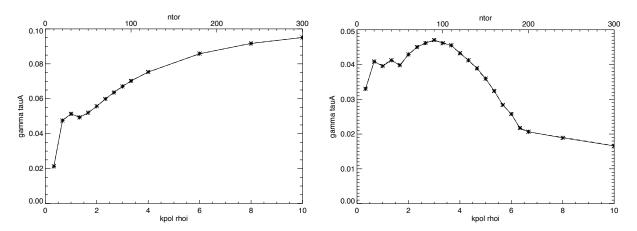

Figure 32. Linear growth rates for the high current Ip=1.0 MA NSTX discharge #128797: (a) resistive ballooning mode model, (b) diamagnetic stabilization model of the vorticity equation.

Completion of the 4th Quarter Milestone

Milestone: Quantify prediction for the divertor heat flux width scaling under moderate particle recycling conditions

The fourth quarter milestone was met by performing simulations of discharges, from all three US tokamaks, selected from the remaining pool listed in the first quarter section of this report. As is required for the present research target, all discharges have a moderate amount of recycling and attached divertor plasmas. The calculations employed moderate (BOUT++, fluid) to extreme scale (XGC1, kinetic) computers. The XGC1 and BOUT++ teams utilized different sets of discharges to satisfy their own requirements and objectives. The BOUT++ work was focused on the effect of electromagnetic fluctuations, while the XGC1 effort targeted the effects of electrostatic blobby turbulence. The XGC1 results yielded excellent quantitative agreement with the experimental divertor heat flux scaling, increasing the level of confidence in the code's predictive capability. The BOUT++ simulations resulted in good agreement with the experimental scaling, apart from an off-normal result in the high current (1.5MA) DIII-D case, as long as the sheath potential was turned off.

1)   XGC1 study

In order to span the full range of relevant poloidal magnetic fields, evaluated at the outboard midplane separatrix (denoted as $B_{pol,MP}$ or B_{pol}), the Q4 simulations incorporated the lowest $B_{pol,MP}$ shot (NSTX #132368, $B_{pol,MP}$=0.20T) and two higher $B_{pol,MP}$ shots (C-Mod #1100223026, $B_{pol,MP}$=0.50T; and C-Mod #1100223012, $B_{pol,MP}$=0.67T). Two medium $B_{pol,MP}$ cases (DIII-D #144977, $B_{pol,MP}$=0.30T; and DIII-D #144981, $B_{pol,MP}$=0.42T) were examined previously, as was the highest $B_{pol,MP}$ discharge (C-Mod #1100223023, $B_{pol,MP}$=0.81T). These six cases nicely cover the full range of $B_{pol,MP}$ values reported by existing tokamak experiments, not just in the US, but worldwide. The discharges simulated with XGC1 are summarized in Table II.

Shot	Time (ms)	B_T (T)	I_P (MA)	$B_{pol,MP}$ (T)
NSTX 132368	360	0.4	0.7	**0.20**
DIII-D 144977	3103	2.1	1.0	**0.30**
DIII-D 144981	3175	2.1	1.5	**0.42**
C-Mod 1100223026	1091	5.4	0.5	**0.50**
C-Mod 1100223012	1149	5.4	0.8	**0.67**
C-Mod 1100223023	1236	5.4	0.9	**0.81**

Table II. The XGC1 simulated discharges from all three large US tokamaks, spanning almost the full range of poloidal magnetic field strengths reported by tokamak experiments worldwide.

1.A) XGC1 study of the medium current C-Mod discharge #1100223012, 0.8MA

The XGC1-simulated parallel heat flux footprint is recorded at the entrance to the Debye sheath of the outer divertor target, after the plasma has traversed the pre-sheath, and then mapped along surfaces of constant Ψ_N back to the outboard midplane. The result for the medium current C-Mod discharge shot #1100223012 (0.8MA, $B_{pol,MP}$=0.67T) is shown in Fig. 33. Application of the Eich fitting formula yields λ_q = 1.14 mm, close to the value obtained from the experimental regression using the method #14 in [Eich2013], $\lambda_q^{(14)} \approx 0.63\ B_{pol}^{-1.19}$ mm = 1.01 mm. The simulated and observed profiles are compared in Fig. 34. The λ_q determined directly from the

experimental profile is $\lambda_q = 0.56$ mm. This is smaller than the Eich regression value due to a diagnostic artifact that broadens the footprint into the private flux region, raising the spread factor S and, thus, reducing λ_q, as explained in [Eich2016].
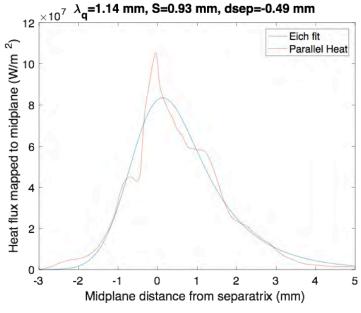

Fig. 33. Diverter heat flux footprint for C-Mod shot #1100223012, 0.8MA, simulated by XGC1 (red line) and the corresponding Eich formula fit (blue)
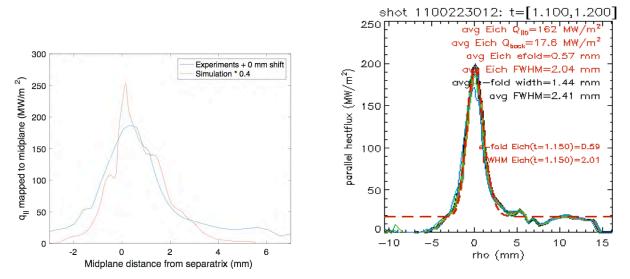

Fig. 34. The divertor heat flux footprint for C-Mod shot #1100223012 obtained by XGC1 (red line in left figure, λ_q=1.14mm) is compared with the experimental result (blue line, left figure). The experimental footprint has an extra spread into the private flux region that is not present in the XGC1 profile, increasing the spread parameter S and, thus, yielding smaller λ_q (=0.57mm, right figure). The extra spread into the private flux region in the experimental footprint is possibly from an IR viewing angle error.

23

Saturation of the simulated heat flux width after 0.65ms is depicted in Fig. 35. The electron heat flux in this simulation has a width comparable to that of the total and is stronger than that of the ion heat flux (Fig. 36), without taking into consideration of the strong neutral particle effect near the divertor plates, indicating that blobby turbulence is playing a significant role. However, the widths of both components are comparable to that obtained from the experimental regression so that ion orbit broadening effects cannot be neglected.
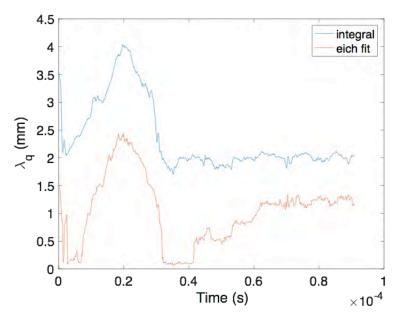

Fig. 35. Saturation of λ_q in the XGC1 simulation after 0.06ms for C-Mod shot #1100223012
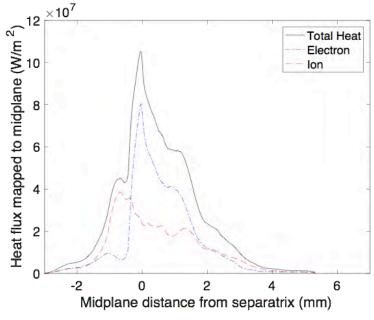

Fig. 36. The width of the simulated electron heat flux in C-Mod shot #1100223012 is comparable to that of the total and greater than that of the ion heat flux, indicating that blobby turbulence is playing a significant role.

1.B) XGC1 study of the low current C-Mod discharge #1100223026

Figure 37 compares the XGC1 simulated divertor heat flux footprint for the low current (0.5MA, B_{pol}=0.5T) C-Mod shot #1100223026 (red line) with the associated fit to the Eich expression (blue), which yields λ_q=1.41mm. The simulated (red line in left figure) and observed (blue line in left figure) profiles are compared in Fig. 38. In this low current discharge, the experimental profile does not exhibit the wider spread into the private flux region noted above, resulting in much better agreement between the experimental (λ_q=1.55mm, right figure), XGC1-simulated (λ_q=1.41mm), and regression widths ($\lambda_q^{(14)} \approx 0.63 \ B_{pol}^{-1.19}$ mm=1.44mm) than in the higher current cases.
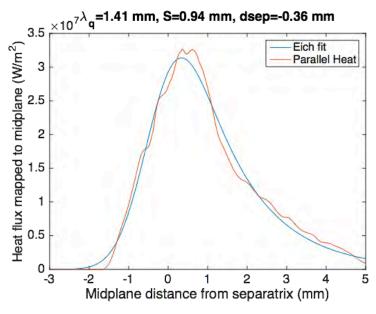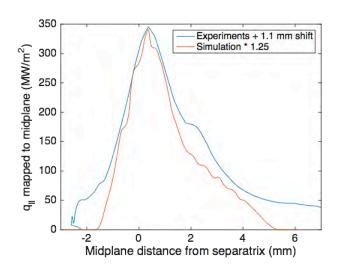

Fig. 37. Divertor heat flux footprint for the XGC1 simulation of the C-Mod low current (0.5MA) shot #1100223026 (red line) and the associated Eich formula fit (blue).
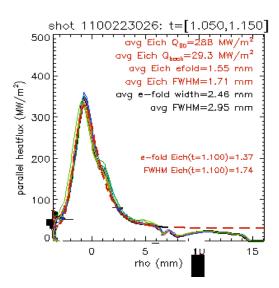

25

Fig. 38. The divertor heat flux footprint for the low current (0.5MA) C-Mod shot #1100223026 from XGC1 (red line in left figure, λ_q=1.41mm) is compared with the experimental footprint (blue line, left figure). In this low current discharge, the experimental profile does not exhibit a wider spread into the private flux region than the XGC1 footprint, resulting in much better agreement among the experimental (λ_q=1.55mm, right figure), XGC1-simulated (λ_q=1.41mm), and regression widths (λ_q=1.44mm).

Figures 39 (left) shows that the integral λ_q obtained from the XGC1 simulation for the low current C-Mod shot (0.5MA, B_{pol}=0.5T) saturates after 0.08ms. However, the width derived from the Eich fitting formula decays following an initial stabilization at 0.1ms, indicating that the profile is shifting inward towards the private flux region. This is believed to be an inaccurate result from excessive neoclassical magnetic drift into the private flux region caused by the grounding of the mean potential to zero along magnetic field-lines in the private flux region considering the short wall-to-wall distance along the field lines, as explained earlier. The Eich λ_q is obtained by averaging these values over all times > 0.08 ms. Figure 39 (right) shows the decomposition of the total divertor heat flux profile into electron and ion components without any smoothing and without taking into account of the strong neutral particle effect near the divertor plates. The peak electron heat flux is greater than that of the ions, but the ion profile is the wider of the two. When combined with the result depicted in Fig. 36, this suggests that the phenomenon predominantly determining the heat flux width shifts from ion-neoclassical to blobby turbulence somewhere between 0.5MA and 0.8MA.
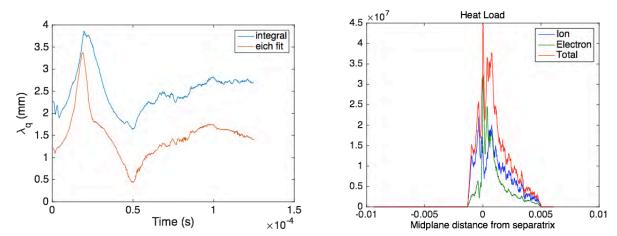

Fig. 39. Left: *The integral λ_q obtained from the XGC1 simulation for the low current C-Mod shot (0.5MA, B_{pol}=0.5T) saturates after 0.08ms. However, the width derived from the Eich fitting formula decays following an initial stabilization at 0.1ms, indicating that the footprint is shifting inward towards the private flux region. This is believed to be an inaccurate result from excessive neoclassical magnetic drift into the private flux region caused by the grounding of the mean potential in the whole private flux region. Right: Decomposition of the total divertor heat flux profile into the electron and ion components without any smoothing (raw data) and without taking into consideration of the strong neutral particle effect near the divertor plates.*

1.C) XGC1 study of the low current NSTX #132368 with I_p= 0.7MA and B_{pol}=0.2T

This simulation represents the extension of the milestone research to the lowest poloidal magnetic fields explored in major present-day tokamaks. In the NSTX geometry, it is also the most difficult case to simulate due to the extremely large magnetic drift effects on the ion orbits and the large flux expansion factor between the high field and low fields regions. As can be seen in the following figures, non-negligible errors are expected.

Figure 40 (left) shows the XGC1 simulated divertor heat flux profile, including a significant spread into the private flux region. This is again due to XGC1's grounding of the mean electrostatic potential in the private flux region. With this assumption, ions can drift into the private flux region without any resistive response by the polarization reaction. Since this behavior has not been seen in other geometries, the large magnetic drifts in NSTX may be to blame. Decomposition of the divertor heat flux into electron and ion contributions (Fig. 40, right), without considering the strong neutral particle effect near the divertor plates, confirms that the excessive spreading into the private flux region is indeed caused by the ions. As a result, the spread factor S in the Eich's fitting expression is larger than it otherwise would be, and λ_q is correspondingly reduced. Since we cannot quantify this error, we include this case in the overall scaling results without any prejudice. The experimental λ_q is 5.5mm, which also has a larger error bar than the higher current cases.
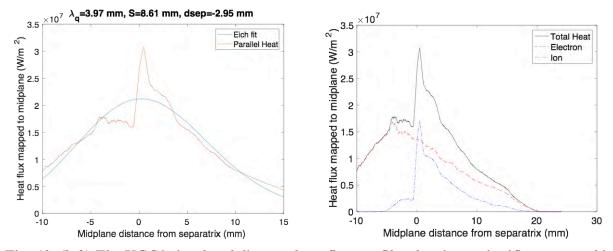

Fig. 40. (left) The XGC1 simulated divertor heat flux profile, showing a significant spread into the private flux region. (right) Decomposition of the heat flux profile into ion and electron contributions, without considering the strong neutral particle effect near the divertor plates, shows that the excessive spreading into the private flux region is caused by the ions.

The heat flux width in this simulation saturates quickly, after only ~0.03 ms (Fig. 41). Experimental heat-flux footprint in this case is shown in Fig. 42, which does not show a large spread into the private flux region.
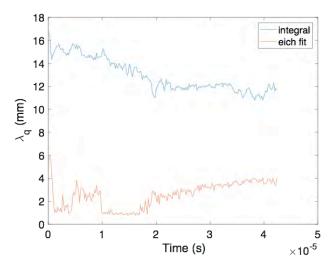
Fig. 41. Quick saturation of λ_q after t~0.03ms in this lowest poloidal field XGC1 simulation of NSTX shot #132368 (I_p= 0.7MA, B_{pol}=0.2T).
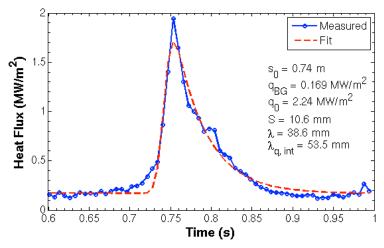

Fig. 42. Experimental divertor heat-flux footprint for the lowest current NSTX shot #132368 with I_p= 0.7MA and B_{pol}=0.2T. This figure is different from other experimental footprint figures in that it is plotted at the divertor plates and not mapped back to the outboard midplane. Thus, the numbers shown in this figure are not to be compared with other numbers presented in this report.

1.D) Quantification of the XGC1 predicted divertor heat flux width scaling under moderate particle recycling conditions

Figure 43 shows the simulation results overlaid on the experimental λ_q data as a function of $B_{pol,MP}$, with Eich's regression represented by the solid line, scaling like $1/B_{pol}^{1.19}$. The experimental data are from [Eich2013]. All six simulations yield divertor heat flux widths that are within the experimental error range, depicted by the adjacent dashed lines.

Figure 43 demonstrates a successful validation of XGC1 in simulating the divertor heat flux width and that it is ready to perform predictive simulation of future devices, such as ITER.
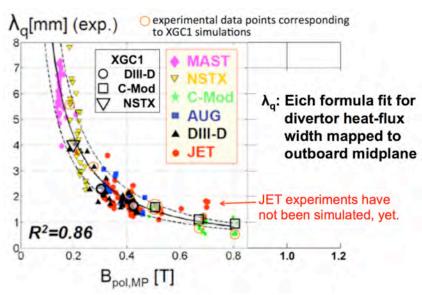
λ_q[mm] (exp.)   ○ experimental data points corresponding to XGC1 simulations

λ_q: Eich formula fit for divertor heat-flux width mapped to outboard midplane

JET experiments have not been simulated, yet.

$R^2=0.86$

Fig. 43. Simulation data overlaid on Eich's experimental data set [Eich2013]. The solid line represents Eich's $1/B_{pol}^{1.19}$ regression formula.

Note that the contributions of blobby turbulence to the heat flux width begin to become significant for poloidal magnetic fields greater than $B_{pol}=0.5T$, according to the XGC1 simulation. Below $B_{pol}=0.5T$, blobby turbulence is not a dominant factor, but the neoclassical ion magnetic drift is. At $B_{pol}>0.5T$, the C-Mod result shows substantial spreading due to blobby turbulence, but the electron heat flux width is still comparable to that of the ions, indicating a cross-over to the blob-dominated regime. As an activity outside of this FES 2016 Milestone Target research, XGC1 has been used to predict λ_q for ITER. The result is a heat flux width driven primarily by blobby turbulence and having λ_q =5.6 mm, over 6 times larger than the width ≲1mm predicted by the empirical scaling formula. With λ_q =5.6 mm, ITER operation would be vastly simpler, requiring only a partially detached divertor instead of the more unwieldy fully detached regime. The plasma operating range would also be much wider and flexible. It appears that there is a hidden device-size parameter missing in the existing regression formulas.

It can be seen from Fig. 43 that JET at higher B_{pol} =0.7T may already be in the blobby turbulence dominated regime. JET is the closest tokamak to ITER among the magnetic fusion devises in operation at the present time. It will be highly desirable to simulate these discharges in the future using XGC1 if more extreme-scale computing resources are available. These simulations could bring an understanding in the size scaling and yield a better analytic formula that can accurately scale to ITER and fusion reactors.

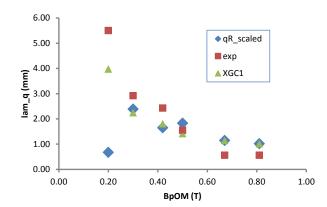It is interesting to note that the XGC1 produced heat-flux widths and the

Fig. 44. Comparison of the XGC1 data against qR scaling.

experimental data follows a simple qR scaling, except for the NSTX discharge (see Fig. 44). More discussions on this can be found at the end of BOUT++ section. It can be argued using Fig. 44 and Ref. [Myra15, Myra16] that a turbulence model could also explain the $1/B_{pol}$ scaling of DIII-D and C-Mod heat-flux width, but not of NSTX heat-flux width, if we assume that the perpendicular diffusion is given by a common turbulence mechanism and the heat-flux spread is proportional to the connection length.

2) BOUT++ study

To understand the role of turbulence on scaling of tokamak divertor heat flux profile widths, we have conducted BOUT++ 6-field two-fluid simulations for a set of experimental plasma profiles relevant to the B_{pol} scan (equivalently, to the I_p scan) at a fixed toroidal magnetic field B_t for C-Mod, DIII-D and NSTX, as well as EAST discharges. All cases are for attached divertor plasma operation.

In the simulations, BOUT++ is interfaced both with kinetic EFIT g-files for magnetic equilibria and p-files for experimentally measured plasma profiles inside the separatrix. With special sources inside the separatrix to maintain experimentally measured plasma profiles there as close as possible, the SOL plasma profiles are allowed to freely evolve in the simulations and the sheath boundary conditions are employed. The simulations follow the self-consistent evolution of turbulence, the SOL plasma profiles with self-consistently generated radial turbulent transport. The axisymmetric electric field is assumed to be generated by diamagnetic effects. Although this is not completely self-consistent, the assumption generates zonal flows in a relatively accurate manner. Both flux-limited parallel thermal transport and the ability to add additional radial transport for ion temperature (on the order of neoclassical transport) are implemented to investigate the sensitivity of the results to the assumptions.

The outputs from the BOUT++ simulation are (1) boundary turbulence fluctuations across the separatrix; (2) power across the separatrix; (3) radial and poloidal plasma profiles in the SOL; (4) radial and parallel heat fluxes profiles for each species; and (5) divertor heat-flux amplitude and widths. The quantities can be compared with experiments are (1) boundary turbulence characteristics; (2) divertor heat-flux widths; (3) divertor heat-flux amplitudes.

In summary, the electromagnetic BOUT++ simulations find that (1) simulated divertor heat-flux profile widths are in good agreement with C-Mod and DIII-D experimental measurements, generally following the experimentally measured inverse dependence on the poloidal magnetic field B_{pol} but with some outliers, although the magnitudes of divertor heat fluxes can be varied, depending on the physics models, sources and sinks; (2) The turbulence dominates over magnetic drifts in electron radial transport fluxes for both DIII-D and C-Mod discharges; (3) the large SOL turbulence originates from the peak gradient region in the pedestal and not from local instabilities in the SOL; (4) the magnetic flutter-induced energy transport is about the same as from the E×B drift channel from the underlying electromagnetic turbulence; (5) The electron heat flux dominates the ion heat fluxes on the outer target. There are two possible reasons for the observation that the electron heat flux exceeds the ion heat flux: (i) less power across the separatrix in the ion rather than electron channel, and/or (ii) longer simulation times that span many ion transit times are needed to determine the final level of ion transport. The latter appears to be important because the ion parallel heat flux on the target is still growing and has not yet saturated. In conclusion, the physics addressed in the simulations is very complex, and the simulations have proved to be very challenging. Much more work should be done.

The NERSC Edison and Cori computers have been used to perform the BOUT++ simulations for the FY 2016 FES Theory & Simulation Performance Target: massively parallel simulations to predict divertor heat-load width. In order complete the quarterly milestone, the entire annual allocation of mp2 repository has been exhausted. In the future we plan to continue gathering physics insight by conducting data analysis of these large scale simulations.

The report is organized as follows: Section (1) contains a description of BOUT++ simulations for DIII-D discharges; Section (2) describes the BOUT++ simulations for C-Mod
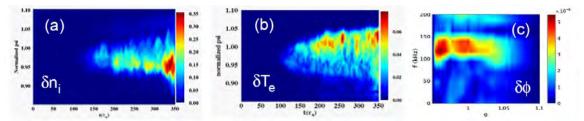

Fig. 1 (a) Ion density fluctuation; (b) Electron temperature fluctuation; (c) spectrogram vs radius

discharges; Section (3) presents the BOUT++ simulations for NSTX discharges; the discussion of time scales and effects due to recycling is given in Section (4); the theoretical analysis is given in Section (5).

(1) BOUT++ Analysis of DIII-D discharges

A set of three DIII-D inter-ELMs H-mode discharges is simulated. The shot numbers are 144987,144977 and 144981. The plasma current is 0.5 MA, 1.0 MA, 1.5 MA, respectively. The radial simulation domain ranges from normalized poloidal flux $\psi = 0.85$ and $\psi = 1.10$, respectively. One fifth of the torus is simulated here for the efficiency. The profiles of three shots are interpolated from EFIT p-files and experimentally measured electric field profiles used. Here the profiles beyond $\psi = 1.0$ are assumed decrease linearly for density and temperature with zero electric field in the SOL.

From the nonlinear simulations, the root-mean-square fluctuation of ion density and electron temperature are shown in Fig. 1 (a) and (b) as contour plots vs radius and time at outer midplane. From Fig.1, we can see that the fastest growing linear unstable modes originate from the peak gradient location in the pedestal, not in the SOL. In the nonlinear stage, the turbulence radially spreads into the SOL and eventually saturates with high SOL amplitude. The steady-state turbulence for electron temperature fluctuations peaks radially around the separatrix at normalized ψ=1.0, and has a broad structure in the poloidal direction for all three cases, even though the ion density and temperature perturbations peak inside separatrix. At the peak turbulence position at the outer mid-plane in Fig. 1, the electron temperature fluctuation is almost in phase with the electric potential, while the density is not, a characteristic drift-Alfven wave feature. FFT analysis shows a predominant wave number $k_\theta \approx 0.8/cm$ for all three current cases and dominant frequencies ≈ 110 kHz, as shown for the three shots in the Table 1. Comparing the spatial and temporal spectra to quasi-coherent modes on C-mod and DIII-D for different discharges, we find similar characteristics, although with different predominant

$k_0 = 0.6/cm$ and frequency f=36 kHz there [D. A. Mossessian, et al., Physics of Plasmas **10**, 689 (2003)]. The poloidal wavenumber k_0 is close to the measured one in [D. A. Mossessian, et al., Physics of Plasmas **10**, 689 (2003)], while the frequency is higher.

Table 1 BOUT++ simulation of turbulence characteristics for DIII-D discharges

Cases	0.5MA	1.0MA	1.5MA
			0.8
Frequency (kHz)	124	110	110

Fig. 2 shows the nonlinearly saturated parallel electron heat fluxes at the outer divertor target for discharge current I_p=1.5 MA. BOUT++ simulation results for the electron parallel heat flux at the divertor target are compared with experimental results in Table 2 and Fig.3 (b) (red squares for DIII-D). In order to compare the heat-flux width with experimental results, we use the same fitting method as used by experimentalists in order to obtain the results shown Fig. 3 (a). Table 2 an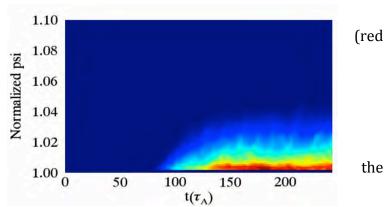d Fig. 3 (b) show that the heat-flux width is comparable to experimental results: almost the same for both 0.5MA and 1.0MA

Fig. 2 Contour plot of divertor parallel electron heat flux versus normalized poloidal flux and time from BOUT++

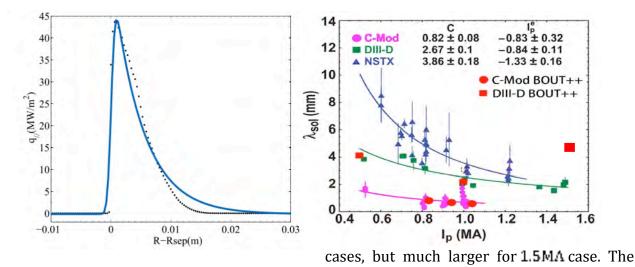
cases, but much larger for 1.5MA case. The

Fig. 3 (a) Parallel electron heat flux versus midplane major radius from BOUT++ (dotted curve) and a fit to the BOUT++ data using the Eich fitting function with parameters as listed Eich fit (solid blue) ; (b) Independent fits of λ_{sol} (or λ_q) versus I_p for each of the three devices. BOUT++ simulated data points for DIII-D (Red square\) and C-Mod (Red period).

possible reason for large width in the high current case is because of the large turbulence amplitude in the SOL region which causes strong radial SOL transport. In our simulations, we use experimentally equilibrium measured electric field profiles, which have zero electric field in the SOL. A more accurate electric field model may suppress the turbulence spreading and possibly yield simulation results closer to experiment. The parallel heat-flux amplitude is also shown in Table 2. The amplitude of the simulation results is about a factor of 3 higher than those in the experimental measurements for all three cases. Possible reasons for this are: (1) a lack of radiative energy losses, (2) the choice of flux-limiting parameter α_j, and (3) the divertor heat flux has not yet reached the steady state. BOUT++ simulations find that the electron parallel heat flux is the dominant contribution to divertor heat flux. More discussion is given in the next section.

Table 2 BOUT++ simulation results and experimental results for DIII-D discharges

case	λ_q(mm)		$q_{\parallel 0}(MW/m^2)$	
	BOUT++	Expt.	BOUT++	Expt.
0.5MA	4.11	3.90	45	13
1.0MA	2.33	2.92	80	27
1.5MA	4.8	2.43	120	34

(2) BOUT++ Analysis of C-Mod discharges

A set of three C-Mod EDA H-mode discharges is simulated. The shot numbers are 1100303017, 1100223023 and 1100223012. The plasma current is 1.0 MA, 0.9 MA, and 0.8 MA, respectively. The radial simulation domain ranges from normalized poloidal flux $\psi = 0.9$ to $\psi = 1.05$, respectively. One fifth of the torus is simulated here for efficiency. The profiles of the three shots are interpolated from EFIT p-files. Here the profiles beyond $\psi = 1.0$ are assumed to decrease linearly for density and temperature. Since there is no electric field profile E_r provided, we determine the E_r profile from force balance with no net flow $E_{r0} = (1/n_0 Z_i e)\nabla P_{i0}$ with ion pressure P_{i0}.
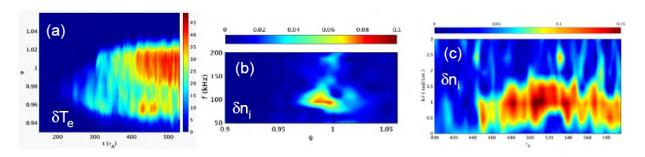

FIG. 4 (a) Contour plot of electron temperature fluctuation vs radius and time at outside midplane; (b) spectrogram vs radius from BOUT++ simulations for quasi-coherent-mode of C-Mod ELMy H-mode; Evolution of poloidal wave-number spectrum for QCMs from BOUT++ simulations. Ip=0.9MA

Table 3 BOUT++ simulation of turbulence characteristics for C-Mod discharges

I_p (MA)	Frequency (kHz)	k_θ (rad/cm)
		1.7
0.9	100	~1.0
0.8	60~120~180	~1.0

The BOUT++ simulations find that the turbulence in C-Mod discharges is localized in the pedestal peak pressure gradient region inside the magnetic separatrix as shown in Fig. 4 and has characteristics of both resistive ballooning modes and drift-Alfven wave instabilities. Figure 4(a) shows the contour plot of electron temperature fluctuations vs radius and time at the outer midplane. The linear instabilities originate at ψ=0.98 at the peak gradient position inside the separatrix and spread into the SOL in the nonlinear regime. Figure 4(b) shows the spectrogram vs radius from BOUT++ simulations, and Fig.
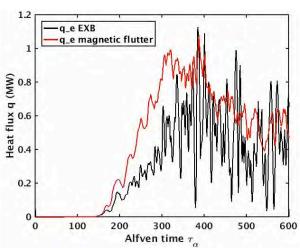

Fig.5 time trace of the magnetic flutter-induced radial energy transport (red curve) and E×B drift induced radial energy transport (black curve) across the separatrix
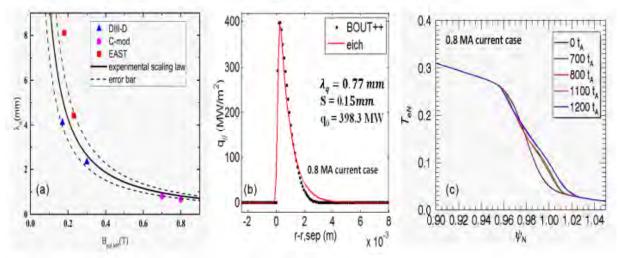

FIG. 6. (a) Poloidal magnetic field at the outer midplane versus heat flux decay length (λ_q) from BOUT++ simulations for DIII-D (blue triangles), C-Mod (violet circles, without the sheath boundary conditions, purple circles with the sheath boundary conditions) and EAST (red squares) . The width determined by a regression for the ITPA multi-machine database to the Eich fitting formula is shown (solid line) as well as error bars for this parameter (dashed lines). (b) Typical outer target power parallel heat flux for BOUT++ simulations and the parameters corresponding to the Eich-fitting formula. (c) Evolution of electron temperature profiles at outer midplane for different times.

4(c) shows the evolution of the poloidal wave-number spectrum. The turbulence amplitudes are maximized near frequency f≈100kHz and poloidal mode number $k_\theta \approx 1$-1.75/cm. These results are very similar in frequency and poloidal mode number to the experimentally measured Quasi-Coherent-Modes (QCMs), and are consistent with experimental measurements. Similar characteristics for the electromagnetic fluctuations are found in our BOUT++ simulations of DIII-D discharges as discussed in the DIII-D section.

The radial transport from the electromagnetic fluctuation consists of two parts: the magnetic flutter-induced energy transport and E×B drift induced energy transport. The magnetic flutter-induced energy transport is proportional to the flux-limiting parallel thermal transport coefficient. Therefore this transport channel plays a more important role for electrons than for ions. Fig. 5 shows that the magnetic flutter-induced energy transport is about the same as that from the E×B drift channel from the underlying electromagnetic turbulence.

The BOUT++ simulations show that the electromagnteic fluctuations cause particles and heat to be turbulently transported radially down their gradients across the separatrix into the SOL, and that parallel transport in the SOL then causes particles and heat to flow towards the divertor. Simulation results for the plasma profiles at outer mid-plane and at the target are shown in Fig. 6. Figure 6(a) shows the heat-flux decay length (λ_q) versus poloidal magnetic field at the outer midplane from BOUT++ simulations for DIII-D (blue triangles) with an outlier at Ip=1.5MA not shown, C-Mod (purple period) and EAST (red square). The solid curve is the result of a regression of the width, using the Eich-fitting formula to the ITPA multi-machine database and the dashed curves show the error bars of the fit. Figure 6 (b) shows a typical outer target parallel heat-flux profile mapped to the outer midplane from BOUT++ simulations and from the result of the Eich-fitting formula. Figure 6 (c) is the typical evolution of the electron temperature profile at outer mid-plane for different times. BOUT++ simulation results are compared with experimental results in Table 4 and Fig.3 (b) (red period for C-Mod for simulations without sheath boundary conditions). It should be noted that both C-Mod data and BOUT++ simulated heat-flux widths on the divertor target are in reasonably good agreement, but they do not follow the scaling of the inverse dependence on the poloidal magnetic field.

Table 4 BOUT++ simulation results and experimental results for C-Mod discharges

I_p (MA)	λ_q (mm)		S (mm)		q0 (MW)	
	BOUT++	Expt.	BOUT++	Expt.	BOUT++	Expt.
1.0	1.38	0.97	0.25	1.07	293	298
0.9	1.35	0.63	0.31	0.93	334	253
0.8	1.39	0.76	0.24	1.22	498	163

It is worth noting that both the BOUT++ and C-Mod results change from those in the third quarter on p.19 for the Ip=0.9MA and Ip=0.8 MA discharges. For BOUT++ simulations, here the simulations are performed with sheath boundary conditions and without neoclassical transport. While on page 19, the simulations are the test runs with different simulation

settings. For the experimental λq for C-Mod, the experimental data on pages 19 is from experiment data base provided, while the experiment data here is from our Eich fitting to the experimental heat flux data as we do for BOUT++ simulation data. They are different.

The power radially transported across separatrix from simulations is consistent with experimental measurements, and is consistent with those reaching the divertor and wall. The energy loss is predominantly to the divertor targets, rather than to the walls.

Finally, the sensitivity of the results to the models and model parameters has been partially investigated. While the simulated heat-flux amplitude could be altered relatively easily, the heat flux width was relatively fixed. The strongest effect observed is that using divertor sheath boundary conditions increases the divertor heat-flux widths by a factor of two. A model of enhanced radial transport has been implemented in the BOUT++ code in order to test the sensitivity to neoclassical vs. turbulent transport. It is found that the divertor heat flux widths do not change much for additional enhanced radial transport on the order of neoclassical transport, which indicates that turbulence is dominant in the simulations. We have tested two different source profiles and locations and find that when the shapes and positions of the sources inside the separatrix are changed, the total heat flux amplitude is changed, but the heat flux width in the SOL is relatively unchanged. Similar effects are observed as the parallel heat-flux limiting parameter α_j is increased from the sheath-limited (α_j =0.05) to free streaming (α_j = 0.8-1.0) value; the simulation results reported above used an intermediate value α_j =0.3, which is close to the theoretical expected value. Since the maximum parallel heat flux is directly proportional α_j, it is found that as α_j is increased, the total power entering the SOL needs to increase in order to maintain the same fixed pedestal temperature. In turn, this leads to an increase in the peak parallel heat flux but only causes small changes in the width. More work will be needed to look into the influence of the various other assumptions in the simulations.

(3) BOUT++ Analysis of NSTX discharges
Simulations that accurately model NSTX discharges are challenging due to the fact that the toroidal magnetic field is relatively weak, the edge q profile is relatively high, and the aspect ratio is low. This implies that numerical resolution requirements are relatively high compared to other tokamak geometries. The toroidal field was B_{tor} = 0.4 T for all cases, which is a factor of 5x smaller than DIII-D and 13.5x smaller than C-MOD, while the plasma currents cover a similar range for all three tokamaks. This implies that the ion gyroradius in NSTX is larger as well. For the highest current case, the gyroradius is approximately 5 mm at the peak pressure gradient location and is similar in size to the minimum pressure gradient scale length of 6 mm. Hence, for an NSTX pedestal, even gyrokinetic models are near their limits of validity at the peak gradient location.

NSTX shot	Time (ms)	P_{NBI} (MW)	B_{tor} (T)	I_p (MA)	λ_q (mm)	S (mm)
132368	360	4	0.4	0.66	7.2	1.7
127975	410	6	0.4	0.94	2.8	0.9
128797	410	6	0.4	1.13	2.1	0.5

Table 5 Key plasma parameters describing the NSTX discharges chosen for analysis

A series of BOUT++ equilibrium meshes, typically with a resolution of 260 radial x 64 poloidal grid points, were generated by using the extended experimental profiles that were provided. The "extended" experimental data smoothly extend over the entire tokamak region, well into the scrape-off layer (SOL). The NSTX discharges that were selected for analysis are described in the table 5. A number of attempts were also made to generate equilibrium files from the pedestal plasma profiles (pfiles), which do *not* provide SOL data and require an extrapolation. However, it was found that this extrapolation tended to cause numerical issues associated with regional boundaries.

Figure 7. Linear growth rates for the high current Ip=1.13 MA NSTX discharge #128797: (a) using the resistive ballooning mode model, (b) using the diamagnetic stabilization model for the vorticity equation. (c) Adding ad hoc damping near the outer boundaries tames the numerical instabilities that arise at low n, although the peak growth rate is reduced by 30%. (d) Adding ad hoc damping near the inner boundary reduces the peak growth rate by an additional 10%.

37

These plasmas are relatively close to linear marginal stability, which makes the initial-value BOUT++ simulations very challenging and nonlinear simulations even more difficult. To ameliorate this issues, the majority of attention was focused on the highest current case, shot 128797 with I_p = 1.13 MA, which has the sharpest gradients and the largest instability drive. Detailed linear stability analysis using the 6-field drift MHD model is shown in Fig. 7. The resistive ballooning model with a realistic Spitzer resistivity profile yields the instability shown in Fig. 7(a) with a relatively small growth rate that is maximized as the toroidal mode # n tends toward infinity and tends toward the value $\sim 0.1/\tau_A$, where the normalization time is τ_A = 2.85×10^{-7} s. After turning on the diamagnetic correction in the vorticity equation, the high n modes shown in Fig. 7(b) are stabilized, and the maximum growth rate γ = $0.047/\tau_A$ = $1.65 \times 10^5/s$ is observed for n = 90. The eigenmodes near the peak in growth rate curve clearly display ballooning structure, as shown in Fig. 8. The
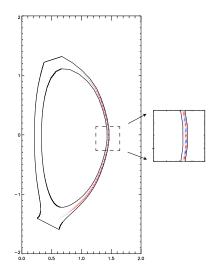

Figure 8. Linear eigenmode structure for toroidal mode number n=100 for the high current Ip=1.13 MA NSTX discharge #128797 using the diamagnetic stabilization model.

modes are driven by gradients in the pedestal, are peaked on the outer midplane, and are dominant on the outer side of the tokamak. Interestingly enough, since the initial state (which is not a true equilibrium) is prepared with poloidally constant profiles, it is found that low n modes (n≤50), have a component in the divertor region that acts to send particles and heat to the target plates.

For both of these scans, numerical issues are observed to pollute the eigenfunctions at low n < 50 and care must be taken in interpreting the results for low n. It was found that these issues could be eliminated by adding ad hoc damping near the outer boundary. This yields the modified growth rate curves in Fig. 7 (c) and (d).

Due to the low toroidal field in NSTX, the poloidal wavenumber of the mode with maximum growth is quite large, $k_{pol} \rho_i \sim 3$, where ρ_i = 5 mm is the value corresponding to experimental measurements in the steep gradient region of the pedestal. This implies that interactions between electron scale and ion scale physics is likely to be important for these cases. This extremely fine-scale structure will stress the capabilities of present gyro-Landau fluid theoretical models which become inaccurate when $k_{pol} \rho_i > 1$.

Over 200 linear BOUT++ simulations (typically using 1024 processors each) of these NSTX discharges have been performed to generate linear growth rate spectra and to investigate the importance of a variety of assumptions and physics models. For example, it was determined that the hyper-resistivity parameter needed to be reduced by a factor of 100x to obtain good performance during linear and nonlinear simulations (from 10^{-13} to 10^{-15} in normalized value). Nonlinear simulations were performed that were based on the most

successful linear runs, but these runs have not yet led to saturated results for the heat-flux-width profile.
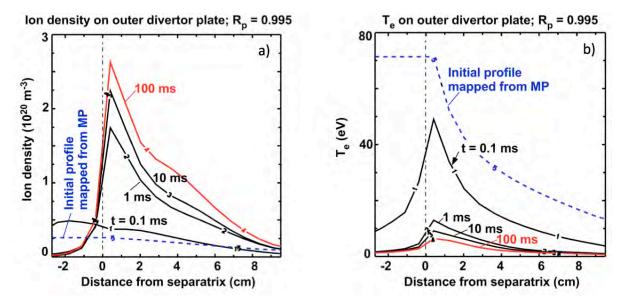

Fig. 9 Plasma density (a) and electron temperature (b) on the divertor plate for a UEDGE transport simulation initialized with poloidally constant SOL profiles and reduced neutral density at t=0 sec. Initial profiles in blue and final in red.

(4) Impact of timescales in the scrape-off layer and divertor heat flux

Because of the strong plasma temperature and density variation between the outer midplane and the divertor region, the full evolution of plasma parameters in this region can occur over times that are significantly longer than the typical BOUT++ turbulence simulations. In order to access the impact of the longer timescales on the plasma and divertor heat flux, a set of basic time-dependent UEDGE transport simulations of this region are performed in a manner similar to the strategy used for the BOUT++ simulations. Initially, a 2D steady-state solution is found for a DIII-D magnetic equilibrium for 2 MW injected plasma power just inside the separatrix at the boundary with the core plasma, and the plasma density there is 3×10^{19} m^{-3}. Anomalous radial
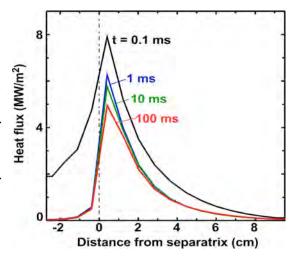

Fig. 10 Heat-flux profiles on the outer divertor plate at various times for conditions and times of the simulations in Fig. 9.

transport coefficients are as follows: for density, D=0.25 m^2/s; for temperatures, $\chi_{i,e}$=1.0 m^2/s; and for radial viscosity of the parallel velocity, $\eta_\perp$=1.0 m^2/s. The particle recycling coefficients on the divertor plates and wall are set to 0.995.

With the steady-state solution in hand, we then reinitialize the simulation using the steady-state profiles in the core region, while in the scrape-off layer (SOL), poloidally constant profiles are used corresponding to the steady-state midplane profiles and the neutral density is reduced by 2 orders of magnitude. This procedure mimics BOUT++'s initialization procedure of using 1D experimental radial profiles at approximately the midplane to initialize the simulation, and again using poloidally constant profiles throughout the SOL. Further, the UEDGE density and temperature values at the core boundary are now fixed to the previous steady-state values, again to follow the BOUT++ effective boundary conditions there.

The results of the UEDGE simulation for plasma density and electron temperature across the outer divertor plate are shown in Fig. 9. The largest temporal variations are in the interval of 0.1-1 ms for both density and electron temperature. This timescale is associated with the parallel ion streaming time between the outer midplane and the divertor plate, a distance of ~25 m and an ion velocity of ~10^5 m/s. Following that time, there is a slow build up of the plasma density by recycling with a concomitant reduction in the electron temperature over a time of 1-100 ms. Note that this later phase is not present in the BOUT++ simulations because recycled neutrals are not included.

Of particular interest for the milestone is the time-dependence of the heat flux on the outer divertor plate. Those profiles are shown in Fig. 10 for the same times given in Fig. 9. Again the largest change is in the range of 0.1-1 ms, but thereafter the heat-flux profiles changes are smaller than that of the separate n_i and T_e profiles in Fig. 9. These results suggest that it is sufficient that the turbulence simulations with self-consistent profile evolution cover a sound transit time of order ~1 ms, although this estimate will likely depend on plasma parameters.

A second set of simulations was performed for a recycling coefficient of 0.5, resulting in low recycling conditions at the divertor plates, which is closer to the BOUT++ simulations that omit recycling. While the divertor values of density and temperature are very different compared to Fig. 9, with the density much lower and the temperature much higher, the divertor plate heat flux profiles are very similar to those shown in Fig. 10. Again, it appears that 1 ms is a sufficient time to approximate the final profile.

(5)   Analytic theoretical estimates of scaling

In Ref. [Myra15] many possible theoretical scaling laws for the heat flux width were obtained depending on details of the underlying turbulence. However, an overall positive scaling of λ_q with connection length $L_{||} \sim qR$, or at least with positive powers of q and R, was found to be a nearly universal feature of the turbulence-driven mechanism. The

reason is that the connection length controls the parallel confinement time of plasma in the SOL: when this time is longer, more turbulent radial transport can occur.

Ref. [Myra15] also showed that an interchange-driven turbulence model (labelled I-BWD in that paper) captured qualitative inter-machine trends of λ_q for present-day machines, while predicting an increasing departure from the Eich scaling for JET and ITER (see Fig. 5 of Ref [Myra15]). The I-BWD model gives $\lambda_q \propto qR^{1/2}L_x^{1/2}/\lambda_p^{3/2}$ where L_x is a radial eigenmode scale and λ_p is pressure gradient scale length in the pedestal region [Myra15]. Further analysis [Myra15] characterizing drift-interchange turbulence in the separatrix region of NSTX using experimental turbulence data has strengthened the connection between λ_q and qR, showing a direct proportionality under some conditions.

Simple cylindrical tokamak estimates give
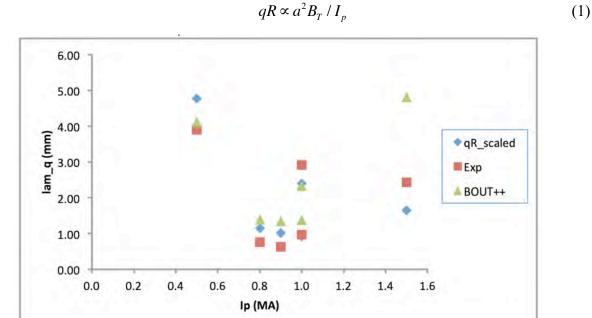
$$qR \propto a^2 B_T / I_p \tag{1}$$

Figure 11 Comparison of λ_q vs I_p for the discharges simulated with BOUT++ showing the experimental measurement (Exp), the simulation result (BOUT++) and the scaling from a simple theoretical estimate (qR_scaled) that is roughly proportional to the connection length.

Parallel heat transport regimes can also affect the scaling of λ_q. Nevertheless, for attached, not too collisional plasmas, it is interesting to see how well the present set of discharge results can be captured by just the connection length effect given in Eq. (1). Figure 11 shows results for λ_q from the experiment, BOUT++ simulations and from the qR scaling. Here $qR_{scaled} = f\, a^2 B_T/I_p$ where the constant scaling factor f = 3.5 was chosen empirically to best match the dataset.

Although the level of agreement may be at least partly fortuitous, it does illustrate several important points. Firstly, it may be difficult to distinguish between neoclassical and turbulence mechanisms from scaling alone, especially from I_p scaling at constant B_T.

Detailed analysis of the turbulence-induced transport is required. Secondly, even if turbulence is not already a significant contributor to λ_q in present day machines, its role is predicted to increase with machine size. These predictions are based on large-scale simulation efforts but are also consistent with simpler analyses [Myra15, Myra16] and even with the connection length effect itself, as illustrated here.

ACKNOWLEDGMENTS

References

[Eich13] T. Eich et al., Nucl. Fusion 53, 093031 (2013)

[Myra15] J. R. Myra, D. A. D'Ippolito, and D.A. Russell, Phys. Plasmas **22**, 042516 (2015).

[Myra16] J.R. Myra, D.A. Russell and S.J. Zweben, "Theory based scaling of edge turbulence and implications for the scrape-off layer width," accepted, Phys. Plasmas (2016).